3. Y. Fukao, *ibid.* **84**, 2303 (1979); A. M. Pelayo and D. A. Wiens, *Geophys. Res. Lett.* **17**, 661 (1990); *J. Geophys. Res.* **97**, 15321 (1992); S. Ide, F. Imamura, Y. Yoshida, K. Abe, *Geophys. Res. Lett.* **20**, 863 (1993); H. Kanamori and M. Kikuchi, *Nature* **361**, 714 (1993); K. Satake, *Geophys. Res. Lett.* **21**, 2519 (1994).
4. H. Kanamori and D. L. Anderson, *Bull. Seismol. Soc. Am.* **65**, 1073 (1975).
5. v_s is defined as the square root of the rigidity divided by the density of the material.
6. Y. Tanioka, L. Ruff, K. Satake, *Island Arc* **6**, 261 (1997).
7. Y. Tanioka and K. Satake, *Geophys. Res. Lett.* **23**, 1549 (1996).
8. I. Kawasaki *et al.*, *J. Phys. Earth* **43**, 105 (1995); K. Heki, S. Miyazaki, H. Tsuji, *Nature* **386**, 595 (1997); K. Heki and Y. Tamura, *Geophys. Res. Lett.* **24**, 3285 (1997).
9. The search of the Harvard CMT catalog used the latitude range of 37° to 43° and longitude range of 140° to 145°. The events were classified as interplate if they met the following criteria: The source depths were less than 80 km; the fault plane, taken from the Harvard fault mechanism solution, had a strike within 20° of the strike of the Japan trench axis (195° ± 20°); and the dip of the fault plane was ≤35°. These criteria for interplate thrust event classification are similar to those used in earlier studies (*2*).
10. The chosen events have seismic moments between 7.24×10^{16} N·m and 4.89×10^{20} N·m, and all recordings are from between 30° and 90° from the events. For more data on the 40 events, see *Science* Online (www.sciencemag.org).
11. All seismic records were deconvolved to displacement traces by removing the instrument response. The mean and linear trend were also removed from the data. The onset of the *P*-wave arrival was then manually selected for all seismograms. Between 4 and 12 recordings were used for each event.
12. The inversion is based on deconvolving a point-source Green function from each signal to extract the moment rate history or source time function. A range of source depths is considered, and the simultaneous fitting of azimuthally distributed signals resolves intrinsic trade-offs between source time function and source depth. For a detailed description of the inversion process, see L. Ruff, *Geophys. Res. Lett.* **16**, 1043 (1989); B. Tichelaar and L. Ruff, *J. Geophys. Res.* **96**, 11997 (1991); L. J. Ruff and A. D. Miller, *Pure Appl. Geophys.* **142**, 101 (1994).
13. The *P*-wave velocity of 6.0 km/s is used as the average velocity from the event hypocenter to the free surface. More complex velocity models for the overthrust wedge can be used for the waveform inversion, such as the model of G. Suarez and D. Comte [*J. Geophys. Res.* **98**, 15825 (1993)]. B. Tichelaar and L. J. Ruff (*ibid.*, p. 15829) showed that the depth estimates vary by <4 km between a simple velocity model and the more complex models, with depths of shallower events tending to be slightly overestimated.
14. The first iteration of the inversion used the source depth listed in the NEIC catalog. Trial depths were then chosen in increments of ±5 km, starting around the first iteration depth, and finer increments of 1 km were used to converge on the optimal depth for the event. The depth is measured from the ocean bottom to the hypocenter.
15. Using the Harvard catalog seismic moments for each event, we normalized the measured source durations to a common seismic moment (M_o) using an empirical relationship [correction = 2.25(log M_o) − 50.7] between the centroid time shift and log seismic moment for all shallow thrust events listed in the Harvard CMT catalog. The durations are normalized to an M_w 6.0 event by adding a constant value to each duration. We are confident that the normalization process removes the magnitude effects on duration, as there is no relation between our normalized duration and log M_o for our data set.
16. In some cases there was a range of depths with low misfit. The source duration listed is for the depth with the lowest misfit, and error bars indicate the depth range giving low misfit.
17. K. Suyehiro and A. Nishizawa, *J. Geophys. Res.* **99**, 22331 (1994).
18. The stress drop is related to the fault displacement divided by fault length or width, along with constants dictated by the crack model. Using the definition for the seismic moment of $M_o = \mu AD = \mu\pi r^2 D$ for a circular crack model (where μ is the rigidity, A is the fault rupture area, r is the radius of the circular fault area, and D is the average displacement on the fault), we calculate the stress drop $\sigma_s = 7\pi M_o/16r^3$. Because the rupture velocity $v = r/t$ excess for a circular expanding rupture, the stress drop is inversely proportional to the cube of rupture velocity (taken to be equal to v_s for simplicity) and the cube of source duration used in Eq. 1.
19. J. E. Vidale and H. Houston, *Nature* **365**, 45 (1993).
20. K. Abe, *Phys. Earth Planet. Inter.* **27**, 194 (1981); *Bull. Seismol. Soc. Am.* **84**, 415 (1994).
21. H. Kanamori, *Phys. Earth Planet. Inter.* **6**, 246 (1972).
22. Y. Tanioka, L. J. Ruff, K. Satake, *Geophys. Res. Lett.* **23**, 1465 (1996); S. Y. Schwartz and L. J. Ruff, *J. Geophys. Res.* **90**, 8613 (1985); J. R. Hartog and S. Y. Schwartz, *Geophys. Res. Lett.* **23**, 2037 (1996).
23. W. Nakayama and M. Takeo, *Bull. Seismol. Soc. Am.* **87**, 918 (1997).
24. R. von Huene and R. Culotta, *Tectonophysics* **160**, 75 (1989); R. von Huene, D. Klaeschen, B. Cropp, *J. Geophys. Res.* **99**, 22349 (1994).
25. P. Vrolijk, *Geology* **18**, 703 (1990).
26. We used the program GMT (Generic Mapping Tools) to generate several of the figures. S. Y. Schwartz, R. Hartog, M. Hagerty, and D. Saffer provided helpful comments on the manuscript. This is contribution number 352 of the Institute of Tectonics, University of California, Santa Cruz. Supported by NSF grant EAR-9418643.

1 April 1998; accepted 2 July 1998

Measurements of the Equation of State of Deuterium at the Fluid Insulator–Metal Transition

G. W. Collins, L. B. Da Silva, P. Celliers, D. M. Gold, M. E. Foord, R. J. Wallace, A. Ng, S. V. Weber, K. S. Budil, R. Cauble*

A high-intensity laser was used to shock-compress liquid deuterium to pressures from 22 to 340 gigapascals. In this regime deuterium is predicted to transform from an insulating molecular fluid to an atomic metallic fluid. Shock densities and pressures, determined by radiography, revealed an increase in compressibility near 100 gigapascals indicative of such a transition. Velocity interferometry measurements, obtained by reflecting a laser probe directly off the shock front in flight, demonstrated that deuterium shocked above 55 gigapascals has an electrical conductivity characteristic of a liquid metal and independently confirmed the radiography.

Hydrogen is the simplest and most abundant element in the universe, yet at high pressure, it is one the most difficult to understand. Having only a single electron, it shows characteristics of both the group I alkalis and the group VII halogens (*1*). At low pressure, hydrogen isotopes are halogenous, covalent diatomic molecules that form insulators. With increasing pressure, the isotopes transform into alkali metals. Although most theories predict <300 GPa for the insulator-metal transition pressure along the 0 K isotherm (*2*), static experiments at even higher pressures have not detected evidence of metallization (*3*). Evidence of high electrical conductivity was observed at an unexpectedly low pressure (140 GPa) at finite temperature (3000 K) where the isotope is in a molecular fluid phase (*4*). There is no accepted theoretical description of the transformation of hydrogen from an insulator into a conducting atomic fluid at high pressures and high temperatures.

G. W. Collins, L. B. Da Silva, P. Celliers, D. M. Gold, M. E. Foord, R. J. Wallace, S. V. Weber, K. S. Budil, R. Cauble, Lawrence Livermore National Laboratory, Livermore, CA 94550, USA. A. Ng, University of British Columbia, Vancouver V6T 1Z1, BC, Canada.

*To whom correspondence should be addressed.

The metallic transition and its effects on the equation of state (EOS) at pressures near 100 GPa are integral to models of many hydrogen-bearing astrophysical objects (*5*), including the Jovian planets (*6*), extrasolar giant planets (*7*), brown dwarfs (*8, 9*), and low-mass stars (*10*), as well as to the design of deuterium-tritium–burning targets for inertial confinement fusion (*11*). The phase space of hydrogen in the vicinity of the finite-temperature insulator-metal transition (Fig. 1) is difficult to address theoretically: it is a dynamic, strongly correlated, partially degenerate composite of H_2, H, H^+, and electrons, as well as other components such as H_3, where no simple approximation is available. This makes reliable experimental data essential as a guide to theory, but meaningful measurements on the Hugoniot (*12*) in this regime have until recently been unattainable. Using a high-power laser, we have accessed this regime by shocking liquid D_2 to pressures at and above the metallic transition where we measured the thermodynamic properties of the shocked state.

At high pressures, molecular dissociation and ionization can be activated through high density as well as thermal effects. Early EOS models either did not include these effects or

predicted that their consequences for the EOS would be small (*13, 14*). More recent theories predict that significant modifications to the EOS can occur either through a continuous dissociative transition (*15*) or a first-order phase transition (*16–18*) from the molecular to the metallic phase.

Shock wave (SW) experiments with light-gas guns have produced Hugoniot data on D_2 (initial density $\rho_o = 0.17$ g cm^{-3}) up to 23 GPa ($\rho = 0.58$ g cm^{-3} and temperature $T = 0.39$ eV), below the transition (*19, 20*). Recently, radiographic measurements were made on the Hugoniot of liquid D_2 near 100 GPa by using a strong shock driven by an intense laser beam (*21*). The sparse data indicated that the shocked density of the isotopes at 100 GPa was much higher than had been predicted by established EOS theories (*13, 14*). The reason was attributed to the effects of molecular dissociation resulting from the high density (*21*).

We used the Nova laser (*22*) to shock liquid D_2 to pressures between 22 and 340 GPa, a wider range of pressure than the earlier experiments. In addition, we verified that this range spans the metal-insulator phase boundary. For each experiment, we determined the SW pressure P and density ρ from measurements of the shock wave speed U_s and the particle velocity behind the shock U_p using the Hugoniot relations $P = \rho_o U_s U_p$ and $\rho = \rho_o U_s / (U_s - U_p)$. Liquid D_2 at 20 K was contained in a 1.5- or 1-mm-diameter, 0.45-mm-long cylindrical cell machined into a copper block. One end of the cell was sealed with an Al or Be disk that acted as a SW pusher and the outside of each pusher was coated with 20 μm of either a polystyrene or Be ablator. The pushers were 180 to 250 μm thick with a root mean square surface roughness of 30 nm for Al and 90 nm for Be. X-ray–transmitting windows consisting of 5-μm-thick Be foils allowed us to perform radiography transverse to the shock direction through the sides of the cell. We also viewed the sample from behind through a 0.5-mm-thick sapphire window. A spatially smoothed Nova laser beam (wavelength λ_L of 527 nm) with an intensity of 10^{13} to 3×10^{14} W/cm^2 irradiated the ablator for 5 to 10 ns. The ablator served to minimize production of high-energy x-rays in the laser plasma. Several laser spot size configurations were used over the course of the shots, from a 400- by 600-μm elliptical spot to a 1-mm-diameter circular footprint. The rapidly heated ablator drove a SW into the metal pusher. Ideally, when the SW reached the rear of the pusher, the pusher-D_2 interface released into the D_2 at the speed U_p while the SW propagated ahead at the speed U_s.

Using transverse radiography, we tracked the positions of the shock front and the pusher-D_2 interface as a function of time to obtain measurements of U_s and U_p for each experiment. The radiography source was a laser-heated Fe foil located 12 cm from the cell. X-rays from the Fe backlight source passed through the cell and into a Kirkpatrick-Baez microscope (bandpass of 800 ± 50 eV) and then into a streak camera. The streak camera slit subtended a strip 300 μm long by 5 μm wide at the target. The slit image was magnified 82 times, resulting in a spatial resolution of 3 μm over the field of view. Two-dimensional hydrodynamic simulations showed that edge rarefactions would attenuate the SW around its periphery. However, the simulations indicated that the SW remained spatially uniform and temporally steady in the center of the SW for sufficient time to obtain accurate data.

The earlier experiments used only Al pushers to obtain a maximum pressure of 210 GPa (*21*). Here we extended the measurements to higher pressure using Be pushers, which have a lower density than Al. The significance of higher pressure is that on the Hugoniot above the metal-insulator transition regime, the compression must eventually approach a value of 4 (*12*). Failure to exhibit this effect would call the experimental meth-

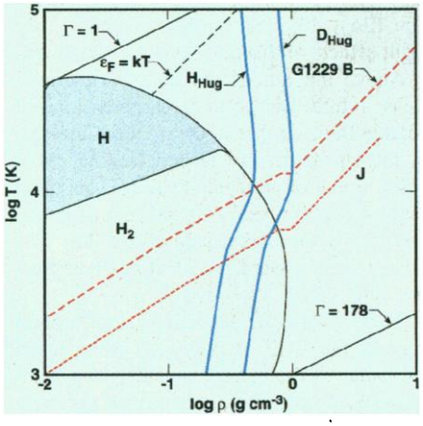

Fig. 1. Model phase diagram of hydrogen (*27*) in the regime of the fluid metal–insulator phase transition. A measure of the interparticle correlation strength is $\Gamma = e^2(4\pi n/3)^{1/3}/kT$, where n is the particle density and k is the Boltzmann constant; a value of $\Gamma > 1$ signifies strong coupling between the fluid constituents and a commensurate lack of simplifying assumptions that enable theoretical calculations. The Fermi energy is ε_F; for temperatures $kT < \varepsilon_F$, matter is partially degenerate. H_2 and H are regions that are mainly molecular and atomic hydrogen, respectively; outside of these regions hydrogen is primarily an ionized fluid. J is a model isentrope for Jupiter (*27*) and G1229 B is an isentrope for brown dwarf G1229 B (*9*). H_{Hug} and D_{Hug} are model hydrogen and deuterium Hugoniots (*12, 15*).

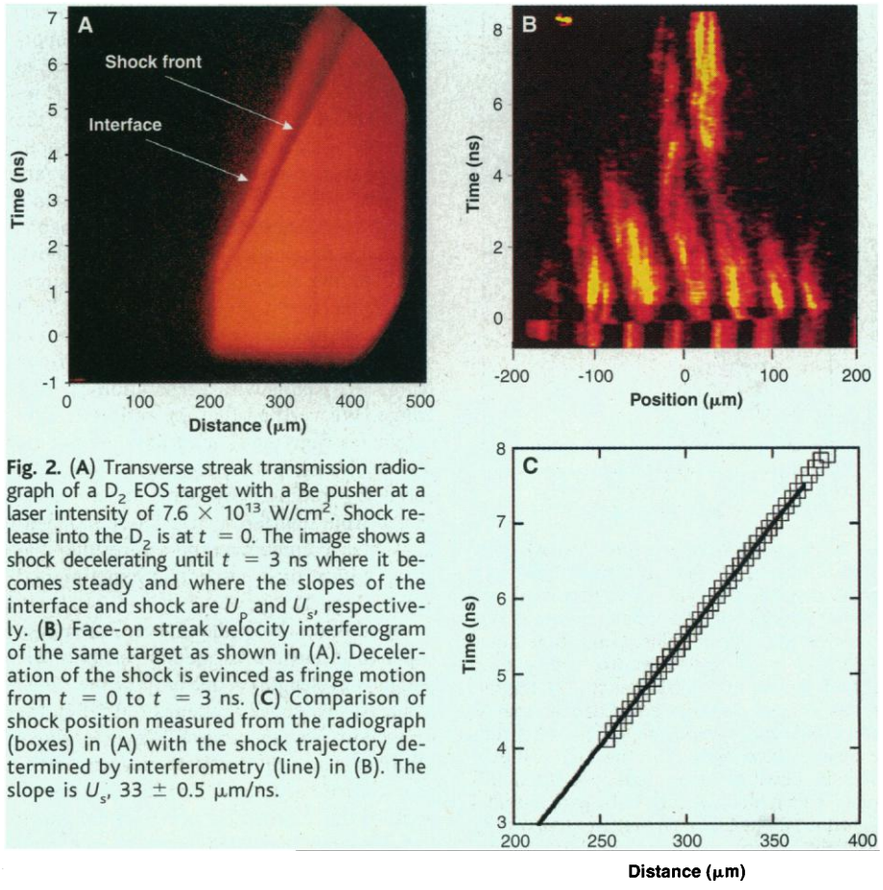

Fig. 2. (**A**) Transverse streak transmission radiograph of a D_2 EOS target with a Be pusher at a laser intensity of 7.6×10^{13} W/cm^2. Shock release into the D_2 is at $t = 0$. The image shows a shock decelerating until $t = 3$ ns where it becomes steady and where the slopes of the interface and shock are U_p and U_s, respectively. (**B**) Face-on streak velocity interferogram of the same target as shown in (A). Deceleration of the shock is evinced as fringe motion from $t = 0$ to $t = 3$ ns. (**C**) Comparison of shock position measured from the radiograph (boxes) in (A) with the shock trajectory determined by interferometry (line) in (B). The slope is U_s, 33 ± 0.5 μm/ns.

odology into question. Because Be is relatively transparent to kiloelectron volt–energy x-rays produced in the laser plasma (and thus more likely to preheat the D_2 sample), we inserted an x-ray–blocking layer of 1-μm-thick Au between the ablator and pusher. The Au did prevent preheating of the D_2, but it also caused SW reverberations in the pusher that were not completely damped by the time the SW released into the D_2. The higher pressure SWs achieved with Be exhibited more temporal variation immediately after release than those produced with Al, resulting in larger uncertainties in measurements of U_s and U_p.

A streak radiograph of shock-compressed D_2 with a Be pusher is shown in Fig. 2A. The pusher is opaque to backlight x-rays, so the interface is the boundary between the light and dark regions. At time $t = 0$, the SW crosses the interface and the interface surface begins to move; by 3 ns, the interface is moving at the final speed U_p. Grazing incidence refraction of backlight x-rays at the density jump across the shock front occurs at angles larger than the acceptance angle of the microscope so that the shock front is visible as a dark line propagating ahead of the interface. The slope of this line is U_s. Absolute uncertainties in U_s and U_p were determined from uncertainties in sweep speed (0.3%), magnification (0.5%), and point selection and deviation of the trajectories from linearity (1%).

The sapphire window at the back of the cell admitted a probe laser. In the original experiments (*21*) the probe was used in a Michelson interferometer configuration, which imaged the rear of the pusher through the unshocked D_2. The interferometer monitored the surface position for evidence of radiative heating of the target. The demonstrated lack of preheating of the sample allowed us to use laser-driven SWs for EOS measurements (*23*).

For these experiments, the probe laser (λ_P = 1.064 μm) was used for velocity interferometry, a technique that measures the Doppler shift of light reflected from a moving surface (*24*). The reflected beam was imaged onto the slit of a streak camera after it was passed through the interferometer. The recorded fringe shift is directly proportional to the Doppler shift and, therefore, to the velocity of the reflecting surface (Fig. 2B). Before SW breakout at $t = 0$, the reflected light originates from the motionless pusher surface, and the fringes are stationary. For $t > 0$, the pattern shifts to a new phase because the reflecting surface is no longer the pusher surface but the shock front moving at U_s in the D_2. The measured velocity is $U_s = \lambda_P F(t)/2\tau$, where τ (= 76.3 ps) is a delay time set by the configuration and $F(t)$ is the fringe count. A shift of one fringe is 7 μm/ns with a resolution of <0.1 fringe. We verified that the reflected light originates from the shock front (and not the pusher) by comparing the trajectories measured by radiography with those determined from interferometry. These independent measurements produced results that agree within their respective experimental errors (Fig. 2C).

In addition to U_s, the interferometer also supplied instantaneous measurements of the (single-wavelength) reflectivity of the shock front. At low shock pressures (20 GPa), the reflectivity is a few percent. However, above 55 GPa the measured reflectivities are ~60%, characteristic of a metal. Because the temperature of the shocked D_2 is ~0.75 eV, much less than the ionization potential, the high reflectivity is due to free electrons produced by a combination of density and thermal effects. In plasma physics, this is referred to as pressure ionization. The temperature is also much less than ε_F (~15 eV), so the term metal is appropriate.

At the lowest compression, the laser data agree with the gas gun results (*19, 20*) (Fig. 3). The most striking feature is the pronounced compressibility observed at the same pressure that D_2 becomes metallic. At 100 GPa, the SESAME (*13*) D_2 Hugoniot density is 0.68 g/cm^3 (ρ/ρ_o = 4), whereas the data show a density of 1.0 g/cm^3 (ρ/ρ_o = 5.88), an increase of 47%. This softer EOS is similar to the models of Saumon-Chabrier (*16*) and Ross (*15*). All of these models use minimization of the free energy of a mixture of molecular, atomic, and ionic species to determine species concentrations and establish thermodynamics of the mixture. The methods and in particular the interspecies potentials are different in each case. Ross uses the expedient of a term determined by gas gun SW data. The Monte Carlo simulations (*17*) are the closest to ab initio, that is, an integration of the interactions of a finite set of individual nuclei and electrons. They show a high compression but at a low pressure. The high-temperature ACTEX model (*25*) also predicts a high shock density. However, the paths to higher pressure of these latter models lie to the low density side of the data. A tight-binding molecular dynamics Hugoniot (*26*), like SESAME, predicts only slight effects of dissociation and ionization.

Above the turnaround on the Hugoniot, D_2 is a fully dissociated, partially ionized metallic fluid, so that as the pressure increases, the shock density is expected to move closer to that of an ideal gas (*12*). This trend was unclear in the original experiments. Here, the compression data above 200 GPa show a trend toward the ideal gas compression (Fig. 3B).

These data offer an independent assessment of the EOS of hydrogen isotopes on both sides of the metal-insulator phase transition. We have seen that hydrogen is ~50% more compressible at the transition than some theories predict (*13, 14, 26*). There is still the question of whether this transition is continuous. The flattened Hugoniots for two EOS models (*16, 17*) are the result of the Hugoniot passing through a predicted first-order phase transition from the molecular to the metallic state (Fig. 3B). The other methods assume a continuous transformation. There is no evidence in the Hugoniot data for a first-order phase transition; shock trajectories and reflectivity display a continuous variation from 25 to 70 GPa. Although there are uncertainties in the data, they suggest that the metal-insulator transition is continuous along the Hugoniot.

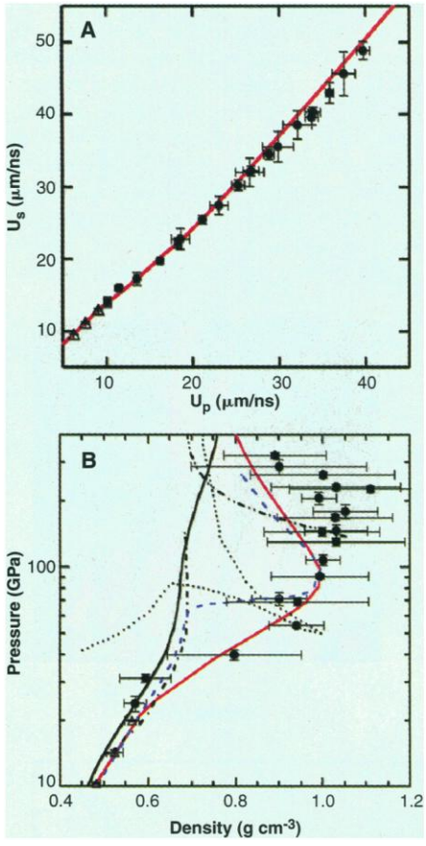

Fig. 3. Hugoniot data presented as (**A**) measured U_s versus U_p and (**B**) inferred pressure versus density. Gas gun data (triangles) are shown (*19, 20*). The EOS model of Ross (*15*) is shown as the solid red line. Other theoretical Hugoniots in (B) are from the widely used SESAME tabular EOS (black solid) (*13*), the hydrogen EOS of Saumon and Chabrier that is used extensively in modeling of low-mass stellar objects (blue dash) (*16*), the ACTEX theory which is known to be accurate at high temperatures (chain double dot) (*25*), path integral quantum Monte Carlo simulations (dots) (*17*), and tight-binding molecular dynamics simulations (dot dash) (*26*).

References and Notes

1. N. W. Ashcroft, *Phys. World* **8**, 43 (July 1995).
2. E. Wigner and H. B. Huntington, *J. Chem. Phys.* **3**, 764 (1935); C. Friedli and N. W. Ashcroft, *Phys. Rev. B* **16**, 662 (1977); T. W. Barbee *et al.*, *Phys. Rev. Lett.* **62**, 1150 (1989); H. Chacham and S. G. Louie, *ibid.* **66**, 10963 (1991).
3. J. H. Eggert *et al.*, *Phys. Rev. Lett.* **66**, 671 (1991); C. Narayana, H. Luo, J. Orloff, A. L. Ruoff, *Nature* **393**, 46 (1998).
4. S. T. Weir, A. C. Mitchell, W. J. Nellis, *Phys. Rev. Lett.* **76**, 1860 (1996).
5. H. M. Van Horn, *Science* **252**, 384 (1991).
6. R. Smoluchowski, *Nature* **215**, 691 (1967); W. B. Hubbard, *Science* **214**, 145 (1981); G. Chabrier, D. Saumon, W. B. Hubbard, J. I. Lunine, *Astrophys. J.* **391**, 817 (1992); W. J. Nellis, M. Ross, N. C. Holmes, *Science* **269**, 1249 (1995).
7. D. Saumon *et al.*, *Astrophys. J.* **460**, 993 (1996).
8. D. Saumon, W. B. Hubbard, G. Chabrier, H. M. Van Horn, *ibid.* **391**, 827 (1992).
9. W. B. Hubbard *et al.*, *Phys. Plasmas* **4**, 2011 (1997).
10. G. Chabrier and I. Baraffe, *Astron. Astrophys.* **327**, 1039 (1997).
11. S. W. Haan *et al.*, *Phys. Plasmas* **2**, 2480 (1995); J. D. Lindl, *ibid.*, p. 3933; S. Nakai and H. Takabe, *Rep. Prog. Phys.* **59**, 1071 (1996).
12. The Hugoniot is the locus of density, pressure, and energy states in a material after passage of a single shock. It is a well-defined curve on the EOS surface. The compression (ratio of shocked to unshocked density) generally increases with pressure and approaches a value of 4 for an ideal gas in the high-pressure limit. The ratio can be greater than 4 when accounting for endothermic processes such as molecular excitations, dissociation, or ionization. At pressures above where these processes are complete, the compression must approach the ideal gas limit. EOSs for hydrogen isotopes are identical except for a scale factor in density.
13. G. I. Kerley, "A theoretical equation of state for deuterium" (Los Alamos Laboratory Rep. LA-4776, Los Alamos, NM, 1972); *J. Chem. Phys.* **73**, 460 (1980).
14. M. Ross, F. H. Ree, D. A. Young, *J. Chem. Phys.* **79**, 1487 (1983).
15. M Ross, *Phys. Rev. B* **58**, 669 (1998).
16. D. Saumon and G. Chabrier, *Phys. Rev A* **44**, 5122 (1991); **46**, 2084 (1992); *Phys. Rev. Lett.* **62**, 2397 (1989).
17. W. R. Magro, D. M. Ceperley, C. Pierleoni, B. Bernu, *Phys. Rev. Lett.* **76**, 1240 (1996); B. Militzer, W. Magro, D. Ceperley, in *Strongly Coupled Coulomb Systems*, G. J. Kalman, K. B. Blagoev, J. M. Rommel, Eds. (Plenum, New York, 1998).
18. H. Reinholz, R. Redmer, S. Nagel, *Phys. Rev. E* **52**, 5368 (1995).
19. W. J. Nellis *et al.*, *J. Chem. Phys.* **79**, 1480 (1983).
20. N. C. Holmes, M. Ross, W. J. Nellis, *Phys. Rev. B* **52**, 15835 (1995).
21. L. B. Da Silva *et al.*, *Phys. Rev. Lett.* **78**, 483 (1997).
22. E. M. Campbell, *Laser Part. Beams* **9**, 209 (1991).
23. Y. M. Gupta and S. M. Sharma, *Science* **277**, 909 (1997).
24. L. M. Barker and R. E. Hollenbach, *J. Appl. Phys.* **43**, 4669 (1972). VISAR, velocity interferometer system for any reflector, is a common term for this technique. These are the first VISAR measurements of shock velocity from a reflecting shock front in motion.
25. F. J. Rogers, *Astrophys. J.* **310**, 723 (1986); ———, F. J. Swenson, C. A. Iglesias, *ibid.* **456**, 902 (1996).
26. T. J. Lenosky, J. D. Kress, L. A. Collins, *Phys. Rev. B* **56**, 5164 (1997).
27. D. Saumon, G. Chabrier, H. M. Van Horn, *Astrophys. J. Suppl. Ser.* **99**, 713 (1995).

28. We thank N. W. Ashcroft, D. M. Ceperley, G. Chabrier, Y. M. Gupta, A. U. Hazi, N. C. Holmes, J. D. Johnson, G. I. Kerley, W. J. Nellis, M. Ross, F. J. Rogers, D. Saumon, T. Tajima, and D. A. Young for informative discussions and J. R. Asay, B. A. Hammel, J. D. Kilkenny, and L. G. Wiley for advice and support. This work was performed under the auspices of the U.S. Department of Energy by Lawrence Livermore National Laboratory under contract number W-7405-Eng-48.

22 April 1998; accepted 10 July 1998

Dimensionality-Driven Insulator-to-Metal Transition in the Bechgaard Salts

V. Vescoli, L. Degiorgi, W. Henderson, G. Grüner, K. P. Starkey, L. K. Montgomery

Optical experiments were conducted on a series of organic linear chain conductors with different values of the interchain single-electron transfer integral t_b, which quantifies the degree of anisotropy. Electron-electron interactions together with Umklapp scattering resulted in a correlation gap and an insulating state for small t_b. An insulator-to-metal transition was observed when t_b exceeded a critical value, on the order of the correlation gap E_{gap}. The absence of a plasma edge on the insulator side of the transition for polarization perpendicular to the chains suggests that the electrons are confined to the chains. The optical features of the metallic state, when contrasted with the magnetic properties, are suggestive of spin-charge separation.

Interacting electrons in reduced dimensions exhibit an enhanced tendency toward the formation of various broken symmetry ground states, whose properties have been explored by various techniques. The "normal" state, that is, the state at temperatures above the transition temperatures of the broken symmetry states, is of interest in part because a strictly one-dimensional (1D) interacting electron system cannot be described by Fermi liquid (FL) theory, the framework of which has been the cornerstone of the theory of interacting electrons in metals and semiconductors for the last half century. The theory is based on the recognition that when interactions can be treated as a perturbation, the low-lying excitations of an interacting electron gas are the same as those of the noninteracting case, only with the energy scales renormalized. FL theory has been thoroughly tested on a variety of materials and is usually valid in higher than one dimension; one well-known exception is the normal state of the two-dimensional (2D) copper oxide–based high-temperature superconductors. The 1D state predicted by the Tomonaga-Luttinger liquid (TLL) theory (*1*) is characterized by features such as spin-charge separation and the absence of a sharp edge in the distribution function at the Fermi wave vector $\mathbf{k}_F$. It has also been suggested (*2*) that for a small transfer integral between chains of interacting electrons, a new state of matter may emerge where the low-lying excitations are confined to the chains and single-electron interchain transfer is not possible but where tunneling of pairs may occur. An analogous scenario has been suggested to occur in high-temperature superconductors. Additional interesting effects arise when the lattice periodicity is involved (*3*, *4*). In this case, electron-electron interactions together with Umklapp scattering result in a correlation gap in the charge excitation spectrum for commensurate band filling (that is, for electron density per unit cell $n = p/q$ with p and q integers). The appearance of this gap also has a marked influence on the interchain electron transfer and on confinement.

The isostructural conductors, based on linear chains of the organic molecules tetramethyltetrathiafulvalene (TMTTF) and tetramethyltetraselenafulvalene (TMTSF), with different interchain counterions X (such as PF_6, ClO_4, and Br), have been the subject of intensive studies recently, to a large extent because of the novel concepts described above. Shortly after they were first synthesized by Bechgaard in 1979, they were found to undergo transitions to various broken symmetry ground states (such as antiferromagnetic, spin density wave, and superconducting states) at low temperatures, typically below 20 K (*4*). The states above the transition temperature, which we will refer to as T_{tr}, are unusual. For example, the resistivity ρ of the $(TMTTF)_2X$ salts has a minimum at a temperature T_ρ, which is in the range ~100 to 300 K. Below T_ρ, but above T_{tr}, ρ increases with decreasing T. In contrast, the

V. Vescoli and L. Degiorgi, Laboratorium für Festkörperphysik, Eidgenössische Technische Hochschule, CH-8093 Zürich, Switzerland. W. Henderson and G. Grüner, Department of Physics, University of California, Los Angeles, CA 90095–1547, USA. K. P. Starkey and L. K. Montgomery, Department of Chemistry, University of Indiana, Bloomington, IN 47405, USA.